DOUBLE-STAGE ACTIVE CONTROL OF MICRO-VIBRATIONS FOR HIGH ACCURACY POINTING MISSIONS

F. Sanfedino[(1)]**, D. Alazard**[(1)]**, N. Guercio**[(2)]**, N. Deslaef**[(3)]

[(1)]*Institut Supérieur de l'Aéronautique et de l'Espace (ISAE-SUPAERO), Université de Toulouse, 10 Avenue Edouard Belin, BP-54032, 31055, Toulouse Cedex 4, France, [francesco.sanfedino, daniel.alazard]@isae.fr*
[(2)]*Thales Alenia Space, Cannes, Provence-Alpes-Côte d'Azur, 06150, France, nicola.guercio@thalesaleniaspace.com*
[(3)]*ESA-ESTEC, Noordwijk, South Holland, 2201 AZ, Netherlands, nicolas.deslaef@esa.int*

ABSTRACT

The increased need in pointing performance for Earth observation and science Space missions together with the use of lighter and flexible structures directly comes with the need of a robust pointing performance budget from the very beginning of the mission design. A multi-body framework, the Two Input Two Output Ports approach, is used to build all the elementary flexible bodies and mechanisms involved in a fine Line-of-Sight mission. A novel control architecture is proposed to reduce the microvibrations induced both by Reaction Wheel (RW) imbalances and Solar Array Drive Mechanism (SADM) driving signal, by keeping them working during the imaging phase. Thanks to a set of accelerometers placed at the isolated base of the payload and at the mirrors with larger size, typically the primary and secondary mirrors of a Space telescope, it is possible to estimate the line-of-sight error at the payload level by blending with the low-frequency measurements of the camera. While a classic Fast Steering Mirror (FSM) in front of the camera can compensate for a large amount of microvibration, an innovative architecture with a set of six Proof-Mass Actuators (PMAs) installed at the payload isolator level can further improve the pointing performance.

1 INTRODUCTION

With the development of the next generation of Earth observation and science Space missions, there is an increasing trend towards highly performing payloads. This trend is leading to increased detector resolution and sensitivity, as well as longer integration time which directly drive pointing requirements to higher stability and lower line-of-sight (LOS) jitter [1]. Such instruments typically comes with stringent pointing requirements and constraints on attitude and rate stability over an extended frequency range well beyond the attitude control system (ACS) bandwidth, by entailing micro-vibration mitigation down to the arcsecond (arcsec) level or less [2][3]. Disturbances induced by internal elements and propagating along the spacecraft large flexible appendages are the main contributor to micro-vibration pointing budget. Among this class of disturbances, two types of internal disturbances can be distinguished from their frequency content: *periodic* or *harmonic* disturbances (like RW static and dynamic imbalances) and *transient* disturbances (like SADM when actuated in particular mission phases). In order to guarantee high pointing performance, it is necessary to entirely characterize the transmission path between the micro-vibration source and the payload. The earlier the model is

available, the easier it is to meet the stringent pointing requirements, by designing appropriate control strategies. The main difficulties encountered in Space system characterization are both the impossibility to correctly identify the system on ground due to the presence of gravity and the consideration of all possible system uncertainties [4].

The possibility to take into account parametric variations in a model fully compatible with the standard robust analysis and control tools opens new insights to design and prototype spacecraft architectures while taking into account all the subsystems (structure modelling, control, optics, mechanism disturbances).

In this spirit the Two-Input Two-Output Ports (TITOP) approach, firstly proposed by Alazard *et al.* [5] and further extended by Chebbi *et al.* [6] and Sanfedino *et al.* [7], offers the opportunity to assemble several flexible sub-structures by keeping the analytical dependency of the overall model on the constitutive mechanical parameters and reducing this dependency to the minimal number of occurrences. This multi-body approach has been conceived in order to perfectly fit with the Linear Fractional Transformation (LFT) theory developed in the robust control framework [8]. It is in fact possible to include any kind of uncertain and varying parameters with a minimum number of occurrences and recover the dynamic (forces and torques) and kinematic (linear and angular accelerations, speeds, displacements) quantities at the connection nodes of each body. In this way, a huge family of possible plants can be incorporated in a unique LFT model that informs the control synthesis algorithm of all possible uncertain and varying parameters. All substructure models derived for simple (i.e. beams and plates) or complex (FEM models of 3D industrial bodies) geometries and mechanisms have been integrated in a MATLAB/Simulink environment using the Satellite Dynamics Toolbox library (SDTlib), a collection of ready-to-use blocks that allows rapid prototyping of complex multi-body systems for space applications [9][10]. The resulting spacecraft model is then ready for robust control synthesis and robust stability and performance assessment by using the MATLAB routines available in the Robust Control Toolbox [11].

The goal of this paper is to show how to finely model an industrial flexible spacecraft with tight pointing requirements and design a robust controller able to push the potential achievable performance to its limits by coping with modeled system uncertainties. In particular an innovative control architecture is presented. It combines multiple passive/active control strategies in order to get a considerable mitigation of the microvibrations induced by RW imbalances and SADM input signals. In particular, combining the measurements of accelerometers in key points of the structure (at the payload isolator base and at the primary and the secondary mirrors of the space telescope) and the low frequency acquisitions of a camera, the LOS is directly corrected by an FSM and indirectly by a set of PMAs installed at the payload isolator level. This strategy allows to get fine pointing performance while leaving the RW and SADM still working during the imaging phase with consequent increase of the time window available for the scientific observations. Indeed, one of the classical but constraining strategies for this kind of missions is to interrupt the operation of the micro-vibration sources in order to improve the pointing performance while having an impact on their primary functionalities (i.e. attitude control for RW, optimization of the received Sun power for the SADM). After outlining the full spacecraft dynamic model in section 2 by assembly of sub-systems using the TITOP framework, section 3 presents the two novel robust control architectures proposed in this work, one relaying on the estimation of the LOS and compensation with an FSM; and the second one based on a set of PMAs controlling an active/passive isolator system placed at the base of the payload. In section 4, results of the analysis are showcased and discussed. Finally, conclusions and remarks are presented in section 5.

2 FULL SPACECRAFT MODELLING

In a spirit of comparing multiple micro-vibration control system architectures, this paper proposes to assess their respective performances (disturbance rejection, stability, robustness) on a dummy space telescope from a generic observation mission. The satellite dynamics can be assembled with the TITOP models derived in the previous sections, in a MATLAB/Simulink environment and the SDT. The proposed spacecraft in Fig. 1 is composed of a central flexible body $\mathcal{B}$ connected to two rotating solar arrays, $\mathcal{A}_1$ and $\mathcal{A}_2$, at points A_1 and A_2 respectively, one flexible optical payload $\mathcal{P}$ and one RWS, respectively connected at two distinct points I_p and I_w. Moreover the payload is anchored at the spacecraft through an isolator assembly as the one presented in Fig. 2 at point I_p. The optical payload is composed of a flexible structure enclosing the optical elements: the two mirrors M_1 and M_2, the charge-coupled device (CCD) and the FSM. The physical parameters of the model, i.e. flexible modes and dampings, are input data from an industrial benchmark, imported in the SDTlib directly with PATRAN/NASTRAN files [10].
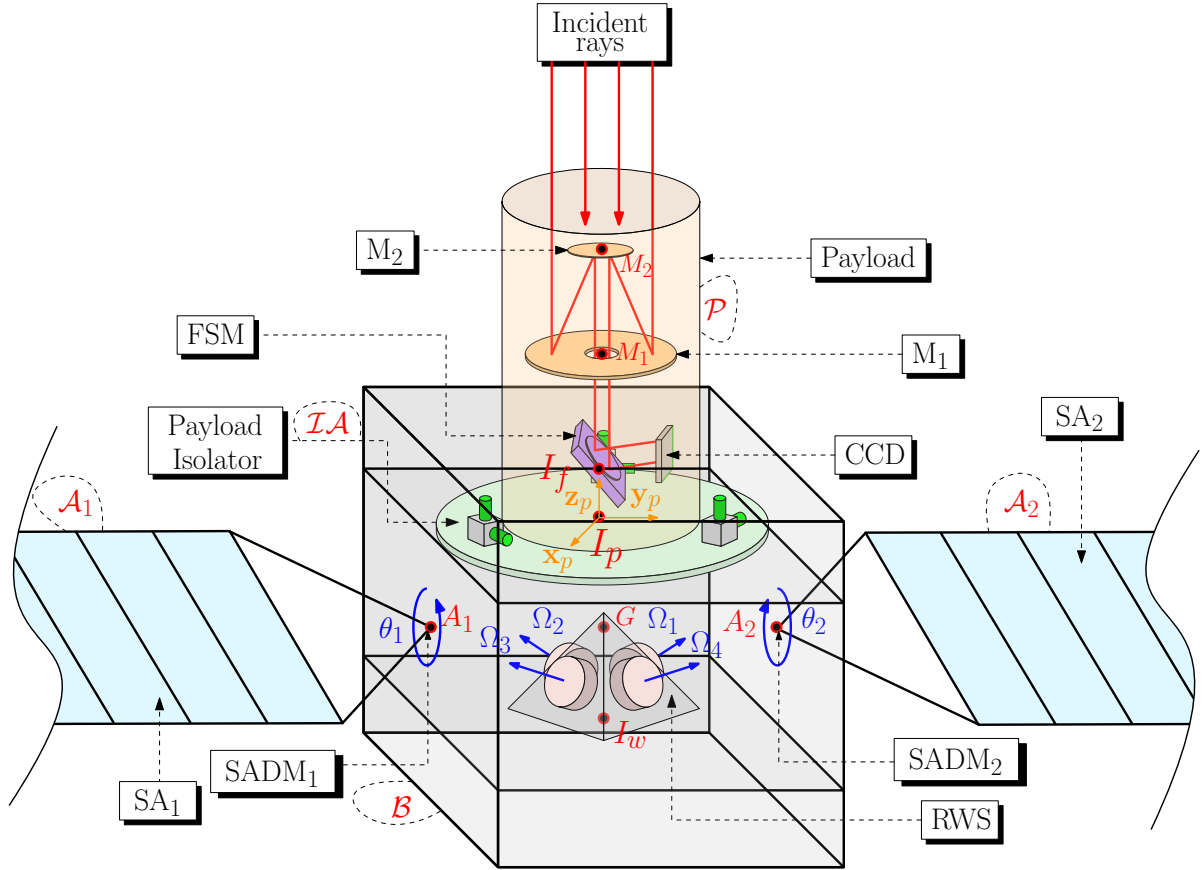
Figure 1: Spacecraft architecture with essential nomenclature

Thanks to SDTlib, it is possible to build the entire spacecraft model by interconnections of elementary blocks corresponding to each sub-structure as depicted in Fig. 3. Note that blocks' colors are the same as each sub-system in Fig. 1. For more details on how to connect several blocks in SDTlib please refer to [12].

In Fig. 3 several models are found:

- $\mathcal{M}^{\mathcal{B}}_{G,I_w,I_p,A_1,A_2}(s)$ is the TITOP model of the flexible central body $\mathcal{B}$ imported from NASTRAN with parent point G (center of mass) and children connection points I_w, I_p, A_1, A_2. The external
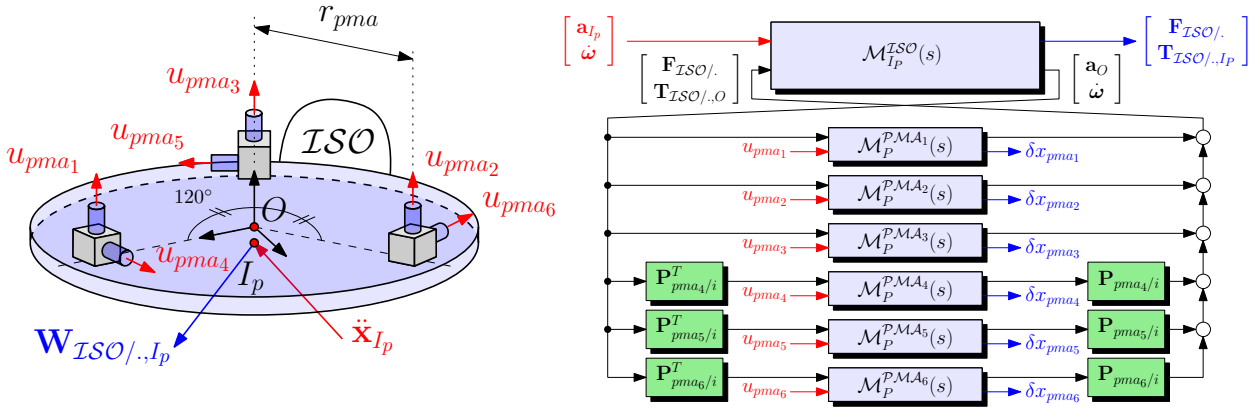
Figure 2: Isolator and PMA assembly (left) and $\mathcal{M}^{\mathcal{IA}}_{I_p}(\mathrm{s})$ TITOP model (right)
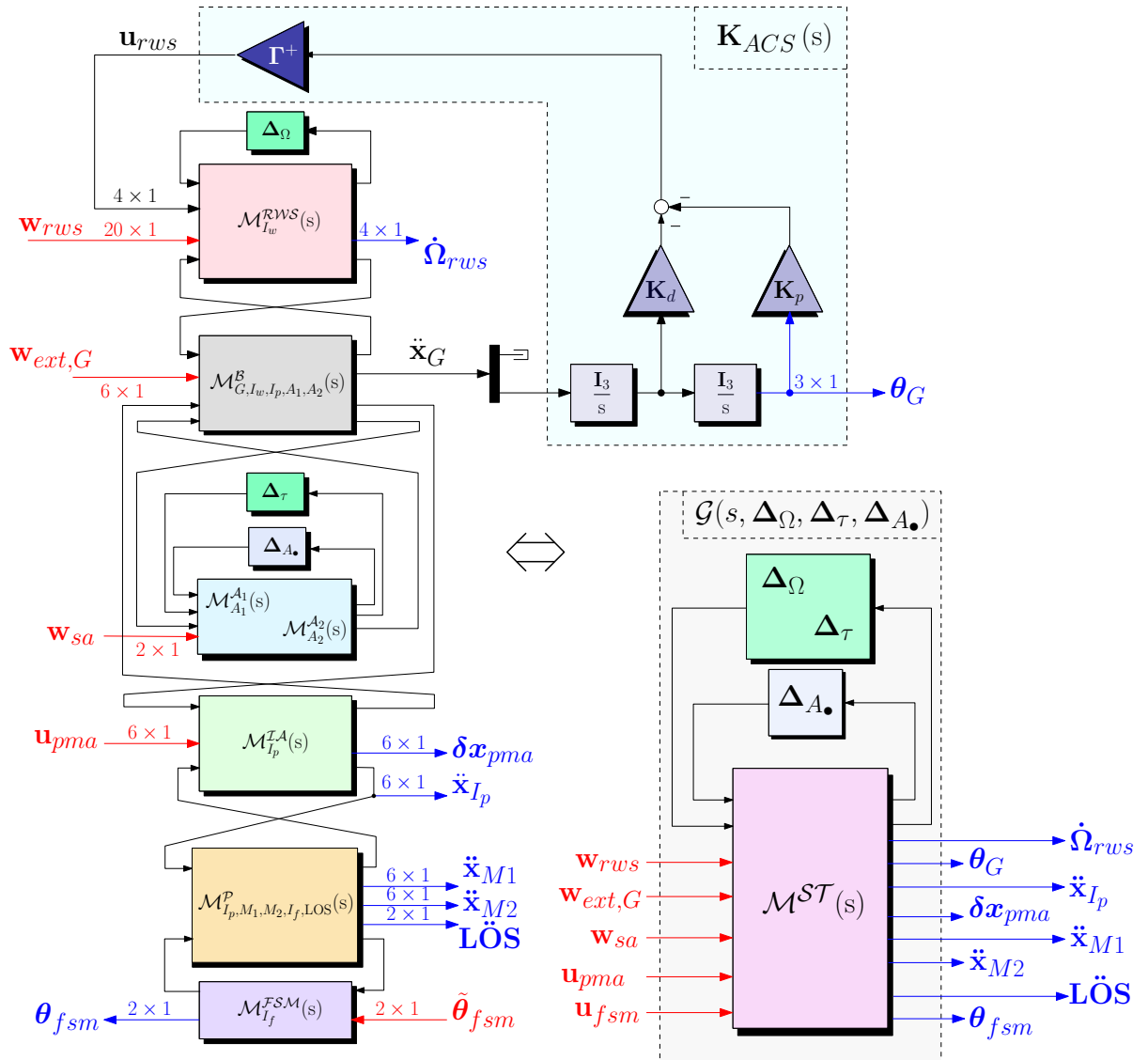
Figure 3: Full space telescope TITOP interconnection diagram (left) and equivalent LFT model (right)

wrench $\mathbf{w}_{ext,G}$ acting at G is the input of this model and the acceleration twist $\ddot{\mathbf{x}}_G$ of the point G is the output;

- $\mathcal{M}_{\mathcal{A}_1}^{\mathcal{A}_1}(\text{s})$ and $\mathcal{M}_{\mathcal{A}_2}^{\mathcal{A}_2}(\text{s})$ are respectively the TITOP models of the two flexible solar panels $\mathcal{A}_1$ and $\mathcal{A}_2$, connected to $\mathcal{B}$ at A_1 and A_2 respectively through two identical SADM, taking into account the stiffness of a reduction gearbox. See [13] for more detail on SADM TITOP model. The block $\boldsymbol{\Delta}_\tau = \tau \mathbf{I}_{32}$ is the parametric uncertainty of the two solar arrays configurations modeling the different orientation of the rotating SA where $\tau = \tan(\theta/4)$ is the parametrization of the SA rotation angle θ presented in [13]. The uncertain block $\boldsymbol{\Delta}_{A_\bullet}$ takes into account the uncertainties on the first two frequencies of the flexible modes of the two SA. $\mathbf{w}_{sa}$ is the vector of the 2 disturbance torques transmitted by the two SADM driving signals to the SA rotation axes;

- $\mathcal{M}_{I_w}^{\mathcal{RWS}}(\text{s})$ is the model of the assembly of four reaction wheels. The block $\boldsymbol{\Delta}_\Omega$ takes into account the four spin rates as varying parameters. The harmonic disturbance vector induced by the four RWs is taken into account in the input $\mathbf{w}_{rws}$;

- $\mathcal{M}_{I_p,M_1,M_2,I_f,\text{LOS}}^{\mathcal{P}}(\text{s})$ is the TITOP model of the flexible payload $\mathcal{P}$ imported from NASTRAN with parent point I_p (connection with $\mathcal{B}$) and children connection points M_1 (connection point with mirror $\mathcal{M}_1$), M_2 (connection point with mirror $\mathcal{M}_2$), I_f (connection point with payload isolator $\mathcal{ISO}$), LOS (connection point with the CCD camera). $\mathcal{M}_{I_p,M_1,M_2,I_f,\text{LOS}}^{\mathcal{P}}(\text{s})$ outputs the acceleration vectors $\ddot{x}_{M_1}$ and $\ddot{x}_{M_2}$ of points M_1 and M_2 respectively and the two angular accelerations $\mathbf{L\ddot{O}S}$ of the LOS, whose double integration is measured by the CCD camera;

- $\mathcal{M}_{P,I}^{\mathcal{IA}}(\text{s})$ is the isolator and PMA asembly showcased in Fig. 2. The 6 PMA control signals $\mathbf{u}_{pma}$ are inputs to this block. The outputs are the acceleration vector $\ddot{\mathbf{x}}_{I_p}$ of point I_p and the six relative displacements $\boldsymbol{\delta x}_{pma}$ of the 6 PMAs;

- $\mathcal{M}_{I_f}^{\mathcal{FSM}}(\text{s})$ is the TITOP model of the FSM. The inputs to this model are the tip/tilt FSM commanded angles $\tilde{\boldsymbol{\theta}}_{fsm}$ and the outputs are the actual tip/tilt FSM angles $\boldsymbol{\theta}_{fsm}$.

For an extensive insight into each of the previous TITOP models the reader is invited to refer to [14]. In order to control the spacecraft attitude, a proportional-derivative (PD) controller tuned on the total inertia matrix (assumed uncoupled) with respect to the central body center of gravity G, $\mathbf{J}^{\text{tot}} = \text{blkdiag}\left(\mathbf{J}_x^{\text{tot}}, \mathbf{J}_y^{\text{tot}}, \mathbf{J}_z^{\text{tot}}\right)$, is proposed:

$$\mathbf{u}_{rws} = -\boldsymbol{\Gamma}^+ \left(\mathbf{K}_d \dot{\boldsymbol{\theta}}_G - \mathbf{K}_p \boldsymbol{\theta}_G\right), \tag{1}$$

where $\mathbf{K}_p = \omega_{\text{ACS}}^2 \mathbf{J}^{\text{tot}}$, $\mathbf{K}_d = 2\zeta_{\text{ACS}}\omega_{\text{ACS}}\mathbf{J}^{\text{tot}}$ (with $\omega_{\text{ACS}} = 0.06$ rad/s, $\zeta_{\text{ACS}} = 0.7$). $\boldsymbol{\Gamma}^+$ is the Moore-Penrose pseudo-inverse of the 3×4 RWS spin axis matrix $\boldsymbol{\Gamma}$ whose columns are the 4 wheels spin axes expressed in the parent (inherited) frame. The total inertia matrix $\mathbf{J}^{\text{tot}}$ can be obtained by computing the inverse low-frequency (DC) gain of the transfer from the body torque disturbances $\mathbf{w}_{ext,G}\{4:6\}$ to the body angular acceleration $\boldsymbol{\theta}_G = \ddot{\mathbf{x}}_G\{4:6\}$. As shown in Fig. 3 the assembled model of the space telescope built in SDTlib is equivalent to an LFT model $\mathcal{G}(s, \boldsymbol{\Delta}_\Omega, \boldsymbol{\Delta}_\tau, \boldsymbol{\Delta}_{A_\bullet}) = \mathcal{F}_u(\mathcal{M}^{ST}(\text{s}), \text{diag}(\boldsymbol{\Delta}_\Omega, \boldsymbol{\Delta}_\tau, \boldsymbol{\Delta}_{A_\bullet}))$. $\mathcal{G}(s, \boldsymbol{\Delta}_\Omega, \boldsymbol{\Delta}_\tau, \boldsymbol{\Delta}_{A_\bullet})$ is an uncertain minimal state-space model of order 204 with 2 occurrences of Ω_1, 2 occurrences of Ω_2, 2 occurrences of Ω_3, 2 occurrences of Ω_4, 4 occurrences of $\omega_1^{A_\bullet}$, 4 occurrences of $\omega_2^{A_\bullet}$ and 32 occurrences of τ.

3 FINE LINE-OF-SIGHT CONTROL

When dealing with microvibrations, the first way to counteract their influence at very high frequency is to use passive isolation. If this strategy allows having an equivalent low-pass filter behavior for high frequencies, on the other hand it introduces some supplementary flexible modes at lower frequencies

as shown in Fig. 4. For this reason, an hybrid (passive + active) control strategy is needed to mitigate microvibrations in the middle range frequencies. Two complementary active control architectures are presented in sections 3.1 and 3.2.
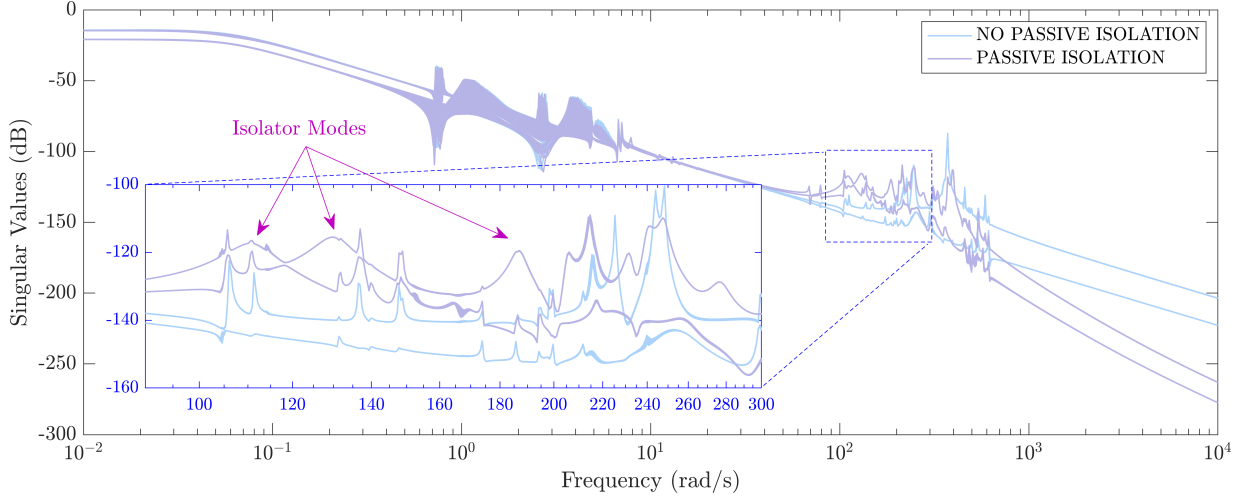
Figure 4: Transmissibility from microvibration disturbance sources (both RW and SADM) to the LOS for the plant $\mathcal{G}(s, \boldsymbol{\Delta}_{\Omega}, \boldsymbol{\Delta}_{\tau}, \boldsymbol{\Delta}_{A_{\bullet}})$ without and with a payload passive isolator

3.1 Hybrid control of LOS with FSM

A piezo-electric FSM is positioned on the optical path of the payload to perform active control at LOS level. Such actuator can perform control over a wide bandwidth, typically ranging from a few Hz to a few hundreds of Hz, which makes it efficient over the entire active control bandwidth. The FSM being controlled in position, one can directly cancel the motion of the LOS by applying the negative of the LOS to the FSM input. The main drawback of such architecture is the need to estimate the LOS at higher frequency than the one offered by direct measurements of a CCD camera $\mathbf{LOS}_c^m$, that does not generally overcome few tens of Hz. For this reason, an estimation of the LOS is done by blending the camera measurements with the measurements provided by the accelerometers (at payload isolator $\ddot{\mathbf{x}}_{I_p}^m$ and at mirrors M_1 and M_2, respectively $\ddot{\mathbf{x}}_{M1}^m$ and $\ddot{\mathbf{x}}_{M2}^m$) and the FSM strain gauges (measuring the FSM tip/tilt deflections $\boldsymbol{\theta}_{fsm}^m$) along the optical path till the CCD camera. The FSM control law is thus an observer-based controller that reads:

$$\mathbf{u}_{fsm} = -\mathbf{S}_{FSM}^{-1} \widehat{\mathbf{LOS}} \tag{2}$$

Where $\mathbf{S}_{FSM} = \mathrm{diag}\,(0.1, 0.1)$ is the FSM sensitivity matrix that relates the motion of the FSM to the LOS, and $\widehat{\mathbf{LOS}}$ is an estimate of the LOS.

The control architecture for FSM robust control synthesis is shown in Fig. 5, where the generalized plant $\mathcal{P}(s, \boldsymbol{\Delta}_{\Omega}, \boldsymbol{\Delta}_{\tau}, \boldsymbol{\Delta}_{A_{\bullet}})$ with normalized input/output weighting filters and the FSM controller $\mathbf{K}_{FSM}(s)$ are depicted. The objective is to obtain the 2×18 dynamic observer $\mathbf{K}_{FSM}(s)$ by ensuring a prescribed level of pointing performance (LOS error) given an expected amplitude of microvibration disturbance as input to the system and coping with FSM actuation authority and all identified model uncertainties and varying parameters. Note that in the diagram a washout filter $\mathbf{F}_w(s)$ is applied to the accelerometer measurements to reject sensor bias:

$$\mathbf{F}_w(s) = \frac{s}{s + 0.1} \mathbf{I}_6 \tag{3}$$

In order to take into account the low-pass behavior of the CCD camera, the filter $\mathbf{F}_{\text{LOS}}$ is used as well:

$$\mathbf{F}_{\text{LOS}}(s) = \frac{100}{s^2 + 14s + 100}\mathbf{I}_2 \tag{4}$$

The set of sensors is characterized by the following levels of white Gaussian noise, with their standard deviations $\boldsymbol{\sigma}$ and sampling times dt:

- accelerometers noise $\mathbf{n}_{a_p}$, $\mathbf{n}_{a_m}$: $\boldsymbol{\sigma}_a = \text{blkdiag}\left(0.0012\,\mathbf{I}_3\,(\text{m/s}^2/\sqrt{\text{Hz}}),\ 0.0023\,\mathbf{I}_3\,(\text{rad/s}^2/\sqrt{\text{Hz}})\right)$, $dt_a = 1\,\text{ms}$;

- CCD noise $\mathbf{n}_{\text{LOS}}$: $\boldsymbol{\sigma}_{\text{LOS}} = 10^{-8}\,\mathbf{I}_3\,(\text{rad}/\sqrt{\text{Hz}})$, $dt_{\text{LOS}} = 1\,(\text{ms})$;

- strain gauge noise $\mathbf{n}_{\text{FSM}}$: $\boldsymbol{\sigma}_{\text{FSM}} = 10^{-8}\,\mathbf{I}_3\,(\text{rad}/\sqrt{\text{Hz}})$, $dt_{\text{FSM}} = 1\,\text{ms}$
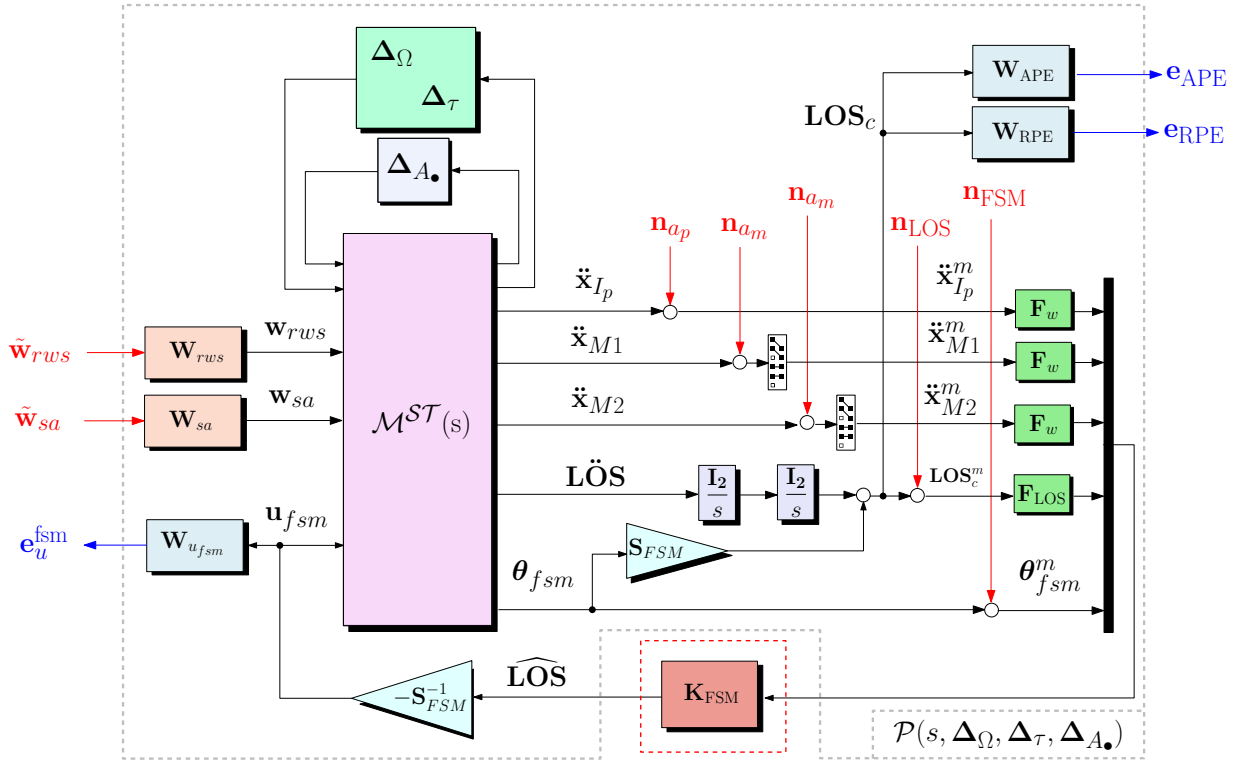
Figure 5: Control architecture for FSM robust control synthesis

For the $\mathcal{H}_\infty$ robust control synthesis, we specify the following input weighting functions:

- $\mathbf{W}_{rws}$ shapes the amplitude of the expected five harmonic perturbations for each of the four RW. For the i-th wheel this filter takes the form:

$$\mathbf{W}_{rws}^i(s) = \text{diag}(0.4\,\text{N},\ 0.4\,\text{N},\ 0.35\,\text{N},\ 0.3\,\text{Nm},\ 0.3\,\text{Nm}) \cdot \frac{s + 5.101 \cdot 10^{-5}}{s + 5.101}\mathbf{I}_5 \tag{5}$$

- $\mathbf{W}_{sa}$ fixes the upper bound of the SADM input disturbance torque:

$$\mathbf{W}_{sa} = 0.1\,\text{Nm} \cdot \mathbf{I}_2 \tag{6}$$

On the other hand, the following output weighting functions have been considered:

- $\mathbf{W}_{\mathrm{APE}}$ bounds the maximum tolerated Absolute Performance Error (APE) [15] on the LOS:

$$\mathbf{W}_{\mathrm{APE}} = \epsilon_{\mathrm{APE}}^{-1}\mathbf{I}_2 \tag{7}$$

In this study $\epsilon_{\mathrm{APE}} = 10\,\mathrm{arcsec}$.

- $\mathbf{W}_{\mathrm{RPE}}$ defines the expected pointing performance in terms of Relative Performance Error (RPE), which is defined in [15] as the angular difference between the instantaneous LOS error vector and the short-time average LOS error vector during a given integration time period t_Δ. In frequency domain the RPE performance corresponds to the high-pass performance weight applied to the LOS error signal:

$$\mathbf{W}_{\mathrm{RPE}}(\mathrm{s}) = \epsilon_{\mathrm{RPE}}^{-1}\frac{t_\Delta\mathrm{s}\left(t_\Delta\mathrm{s} + \sqrt{12}\right)}{(t_\Delta\mathrm{s})^2 + 6\left(t_\Delta\mathrm{s}\right) + 12}\mathbf{I}_2 \tag{8}$$

where ϵ_{RPE} overbounds the maximum RPE target value. For the present study case $t_\Delta = 20\,\mathrm{ms}$ and $\epsilon_{\mathrm{RPE}} = 100\,\mathrm{marcsec}$.

- $\mathbf{W}_{u_{fsm}}$ bounds the maximum available FSM input commands:

$$\mathbf{W}_{u_{fsm}} = \frac{1}{\bar{u}_{fsm}}\mathbf{I}_2, \quad \text{with } \bar{u}_{fsm} = 5.3\,\mathrm{mrad} \tag{9}$$

The robust 4-th order LOS observer is synthesized in an $\mathcal{H}_\infty$ framework using the non-smooth optimization algorithms [16, 17] available in the MATLAB routine *systune*. This approach allows fixed structure low order controllers to be designed by imposing multi-objective optimization criteria and by coping with all parametric uncertainties in the model.

The $\mathcal{H}_\infty$ optimization problem to find the optimal observer $\hat{\mathbf{K}}_{\mathrm{FSM}}(\mathrm{s})$ is formulated as it follows:

$$\hat{\mathbf{K}}_{\mathrm{FSM}}(\mathrm{s}) = \underset{\mathbf{K}_{\mathrm{FSM}}(\mathrm{s})}{\arg\min}\ \underset{\boldsymbol{\Delta}_\Omega, \boldsymbol{\Delta}_\tau, \boldsymbol{\Delta}_{A_\bullet}}{\max} \left\{ \begin{array}{l} \gamma_1 = \left\| \mathcal{F}_l(\mathcal{P}(\mathrm{s}, \boldsymbol{\Delta}_\Omega, \boldsymbol{\Delta}_\tau, \boldsymbol{\Delta}_{A_\bullet}), \mathbf{K}_{\mathrm{FSM}})_{[\tilde{\mathbf{w}}_{rws}^\mathrm{T}\ \tilde{\mathbf{w}}_{sa}^\mathrm{T}]^\mathrm{T} \to \mathbf{e}_{\mathrm{APE}}} \right\|_\infty \\[2mm] \gamma_2 = \left\| \mathcal{F}_l(\mathcal{P}(\mathrm{s}, \boldsymbol{\Delta}_\Omega, \boldsymbol{\Delta}_\tau, \boldsymbol{\Delta}_{A_\bullet}), \mathbf{K}_{\mathrm{FSM}})_{[\tilde{\mathbf{w}}_{rws}^\mathrm{T}\ \tilde{\mathbf{w}}_{sa}^\mathrm{T}]^\mathrm{T} \to \mathbf{e}_{\mathrm{RPE}}} \right\|_\infty \end{array} \right.$$

$$\text{such that:} \quad \gamma_3 = \underset{\boldsymbol{\Delta}_\Omega, \boldsymbol{\Delta}_\tau, \boldsymbol{\Delta}_{A_\bullet}}{\max} \left\| \mathcal{F}_l(\mathcal{P}(\mathrm{s}, \boldsymbol{\Delta}_\Omega, \boldsymbol{\Delta}_\tau, \boldsymbol{\Delta}_{A_\bullet}), \mathbf{K}_{\mathrm{FSM}})_{[\tilde{\mathbf{w}}_{rws}^\mathrm{T}\ \tilde{\mathbf{w}}_{sa}^\mathrm{T}]^\mathrm{T} \to \mathbf{e}_u^{\mathrm{fsm}}} \right\|_\infty < 1 \tag{10}$$

Due to the gradient-based optimization nature of the non-smooth algorithm, it is necessary to find a good initial guess in order to get satisfactory results. This is why before running the $\mathcal{H}_\infty$ synthesis, a linear Kalman filter is synthesized as first guess of $\mathbf{K}_{FSM}(\mathrm{s})$. The simplified model used for the Kalman filter design is shown in Fig. 6: the controlled LOS $\mathbf{LOS}_c$ is modelled by reconstructing the optical path from the accelerometers, the FSM strain gauges and the kinematic models between the sensor locations in the structure and is measured by the CCD camera.

The primary measurements vector (input to the Kalman model) is composed by the inertial measurements from the accelerometers placed on the various elements of the payload, as well as the FSM x and y deflections measurements:

- $\left[\ddot{\mathbf{x}}_{I_p}^m\right]_{\mathcal{R}_P}$ is the acceleration twist measurement at the payload isolator reference point projected in the payload frame $\mathcal{R}_p$,
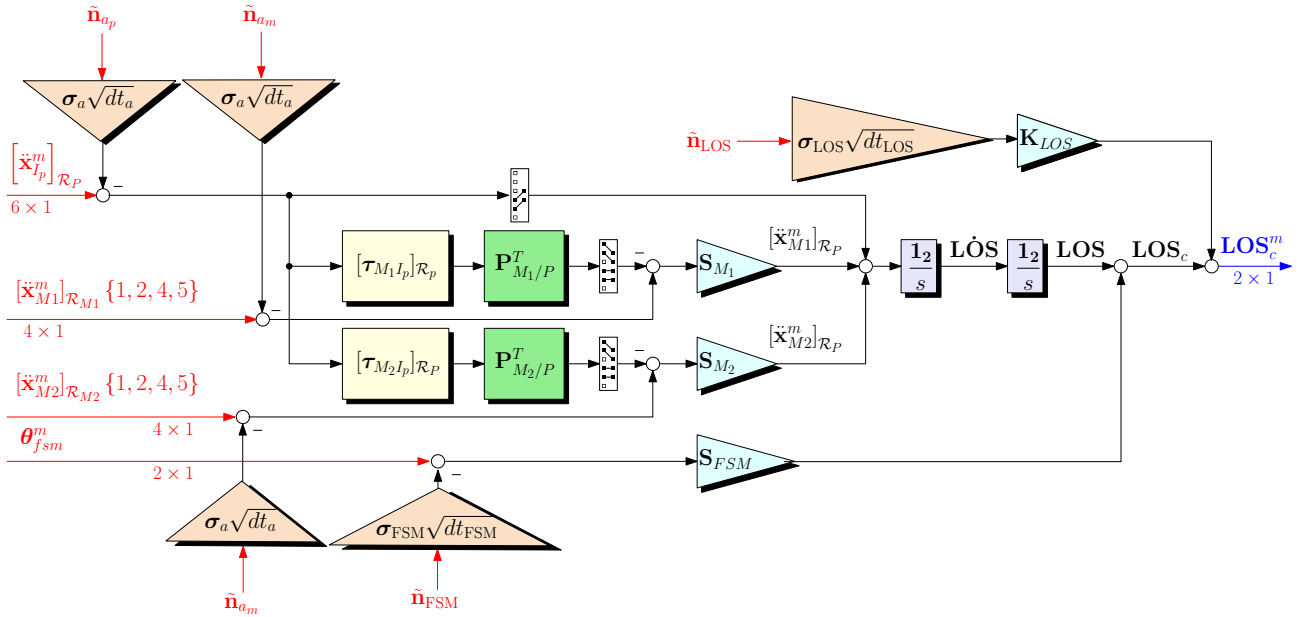
Figure 6: Kalman model for LOS estimation

- $[\ddot{\mathbf{x}}_{M1}^m]_{\mathcal{R}_{M1}}$ is the acceleration twist measurement at the point of the mirror M_1 projected in the mirror M_1 local frame $\mathcal{R}_{M_1}$,

- $[\ddot{\mathbf{x}}_{M2}^m]_{\mathcal{R}_{M2}}$ is the acceleration twist at the point of the mirror M_2 projected in the mirror M_2 local frame $\mathcal{R}_{M2}$,

- $\boldsymbol{\theta}_{fsm}^m$ is the angular position vector measurement of the FSM around the $\mathbf{x}$ and $\mathbf{y}$ axes in the payload frame $\mathcal{R}_p$.

The secondary measurements vector (output of the Kalman filter) is only composed of the LOS reconstruction done via image processing algorithm:

- $\mathbf{LOS}_c = \mathbf{LOS} + \mathbf{S}_{FSM}\boldsymbol{\theta}_{fsm}$ is the controlled LOS.

The Kalman model contains the following kinematic parameters:

- $[\boldsymbol{\tau}_{M_i I_p}]_{\mathcal{R}_p}$ is the kinematic model between the point I_p and M_i (expressed in the frame $\mathcal{R}_p$),

- $\mathbf{P}_{M_i/p}$ is the DCM mapping a vector expressed in the frame $\mathcal{R}_{M_i}$ into a vector expressed in the frame $\mathcal{R}_p$,

- $\mathbf{S}_{M_i}$ is the 2×6 sensibility matrix of the LOS in the payload body frame $\mathcal{R}_p$ to the local deflections of the payload at the point M_i.

The normalized noise inputs $\tilde{\mathbf{n}}_\bullet$ are Gaussian centered white noises with unit power spectral density (PSD).
This Kalman model does not take into account the low-pass behavior of the camera measurements in order to limit the order of the resulting estimator. For this reason the gain $\mathbf{K}_{LOS} = 10^5$ is introduced to degrade the secondary measurement. The resulting filter, denoted $\mathbf{K}_{est}(\mathrm{s}) \in \mathbb{R}^{2\times18}$, is a 4th order linear Kalman filter.

3.2 Hybrid control of LOS with FSM and PMAs

The FSM control loop presented in section 3.1 manages to achieve a broadband rejection of microvibrations. A further reduction of the LOS error can be obtained if a set of six PMAs, connected to the payload isolator, is used in an active isolation feedback loop on the payload acceleration $\ddot{\mathbf{x}}_{I_p}^m$. The control architecture is the one proposed in Fig. 7, where the generalized plant is now $\mathcal{Q}(s, \boldsymbol{\Delta}_\Omega, \boldsymbol{\Delta}_\tau, \boldsymbol{\Delta}_{A_\bullet})$ and the 6×6 controller to be optimized is $\mathbf{K}_{\mathrm{PMA}}$.

Figure 7: Control architecture for PMA robust control synthesis

In this case, a finer RPE requirement than in FSM synthesis is imposed in order to exploit the high-pass filter behavior of the PMAs. We use then the filter:

$$\mathbf{W}_{\mathrm{RPE}}^f(s) = \epsilon_{\mathrm{RPE}^f}^{-1} \frac{t_\Delta s\left(t_\Delta s + \sqrt{12}\right)}{\left(t_\Delta s\right)^2 + 6\left(t_\Delta s\right) + 12} \mathbf{I}_2 \tag{11}$$

where $\epsilon_{\mathrm{RPE}^f} = 40\,\mathrm{marcsec}$ and $t_\Delta = 20\,\mathrm{ms}$. Moreover, the output filter $\mathbf{W}_{u_{pma}}$ overbounds the maximum PMA input force:

$$\mathbf{W}_{u_{pma}} = \frac{1}{\bar{u}_{pma}} \mathbf{I}_6 \tag{12}$$

with $\bar{u}_{pma} = 31.6\,\mathrm{N}$.

The mixed $\mathcal{H}_\infty/\mathcal{H}_2$ optimization problem to find the optimal controller $\hat{\mathbf{K}}_{\mathrm{PMA}}$ is formulated as it follows:

$$\hat{\mathbf{K}}_{\mathrm{PMA}}(s) = \underset{\mathbf{K}_{\mathrm{PMA}}(s)}{\operatorname{argmin}} \max_{\boldsymbol{\Delta}_\Omega, \boldsymbol{\Delta}_\tau, \boldsymbol{\Delta}_{A_\bullet}} \begin{cases} \gamma_1 = \left\|\mathcal{F}_l(\mathcal{Q}(s, \boldsymbol{\Delta}_\Omega, \boldsymbol{\Delta}_\tau, \boldsymbol{\Delta}_{A_\bullet}), \mathbf{K}_{\mathrm{FSM}})_{[\tilde{\mathbf{w}}_{rws}^{\mathrm{T}} \, \tilde{\mathbf{w}}_{sa}^{\mathrm{T}}]^{\mathrm{T}} \to \mathbf{e}_{\mathrm{APE}}}\right\|_\infty \\ \gamma_2 = \left\|\mathcal{F}_l(\mathcal{Q}(s, \boldsymbol{\Delta}_\Omega, \boldsymbol{\Delta}_\tau, \boldsymbol{\Delta}_{A_\bullet}), \mathbf{K}_{\mathrm{PMA}})_{[\tilde{\mathbf{w}}_{rws}^{\mathrm{T}} \, \tilde{\mathbf{w}}_{sa}^{\mathrm{T}}]^{\mathrm{T}} \to \mathbf{e}_{\mathrm{RPE}}^f}\right\|_\infty \\ \gamma_3 = \left\|\mathcal{F}_l(\mathcal{Q}(s, \boldsymbol{\Delta}_\Omega, \boldsymbol{\Delta}_\tau, \boldsymbol{\Delta}_{A_\bullet}), \mathbf{K}_{\mathrm{PMA}})_{\tilde{\mathbf{n}}_{a_p} \to \mathbf{e}_{\mathrm{APE}}}\right\|_2 \end{cases}$$

$$\text{such that:} \quad \gamma_4 = \max_{\boldsymbol{\Delta}_\Omega, \boldsymbol{\Delta}_\tau, \boldsymbol{\Delta}_{A_\bullet}} \left\|\mathcal{F}_l(\mathcal{Q}(s, \boldsymbol{\Delta}_\Omega, \boldsymbol{\Delta}_\tau, \boldsymbol{\Delta}_{A_\bullet}), \mathbf{K}_{\mathrm{PMA}})_{[\tilde{\mathbf{w}}_{rws}^{\mathrm{T}} \, \tilde{\mathbf{w}}_{sa}^{\mathrm{T}}]^{\mathrm{T}} \to \mathbf{e}_u^{\mathrm{pma}}}\right\|_\infty < 1 \tag{13}$$

Note that the $\mathcal{H}_2$-norm objective γ_3 is considered in order to limit the amplification of the accelerometers noise by the minimization of the variance between measurement noise and pointing performance.

4   RESULTS AND DISCUSSION

In this section, the results obtained with the control architectures outlined in section 3.1 and 3.2 are analyzed. Table 1 resumes the achieved optimization performance indexes. One can notice that for the FSM robust control synthesis (optimization problem (10)), the limits of system performance are reached since all indexes reach the unity value). The hard constraint on control authority γ_3 is satisfied by leaving a very small margin for further improvement of the two pointing performance indexes, γ_1 and γ_2. Note that the RPE performance index γ_2 is slightly bigger than unity, fact that is not considered critical for this design. Moreover note that these indexes corresponds to the worst-case achievable performance by taking into account all possible uncertainties and considering the biggest $\mathcal{H}_\infty$-norm on all parametric configurations. The saturation of the three performance indexes means that a further reduction of the LOS jitter cannot be demanded since the limit of performance is already been reached. This limit is in fact imposed both by the physical characteristics (maximum accepted FSM input signal, noise) of the set of sensor/actuators chosen for this control architecture and the need of performance robustness against uncertain/variable parameters.

In order to further improve the jitter rejection, a second stage of micro-vibration active control is added to the already synthesized FSM closed-loop. A set of 6 PMA is then introduced in order to reject the transmitted disturbances to the payload base and improve the performance reached by the FSM. For the synthesis of the PMA controller the optimization problem (13) is solved. Note that this time a reduction of 60 marcsec is asked in terms of RPE performance with respect to the FSM closed-loop synthesis. As shown in Table 1 the more restrictive requirement on RPE performance (γ_2) is met. However only $\approx 12\%$ of the available control signal (γ_4) is sufficient to guarantee the requested pointing performance (γ_1 and γ_2) by coping with a limitation of the accelerometer noise propagation to the LOS (γ_3). This means that a set of PMA with lower maximum available input force could be sufficient to meet the same level of pointing performance. Moreover, one can notice that the APE requirement is largely met ($\gamma_1 = 0.5768$) since the FSM control stage already takes care of it. The biggest limitation in this design is then due to the noise introduced by the chosen set of accelerometers (γ_3).

FSM Synthesis			PMA Synthesis			
γ_1	γ_2	γ_3	γ_1	γ_2	γ_3	γ_4
0.9857	1.0026	0.9877	0.5768	0.9835	0.9835	0.1185

Table 1: Worst-case performance of FSM and PMA robust control design

Figure 8 shows the singular values of the two optimal controllers. Figure 8a compares the final $\hat{\mathbf{K}}_{\mathrm{FSM}}(s)$ with the initial Kalman Filter first guess $\mathbf{K}_{est}(s)$. The FSM controller is of course a 4th order system as its corresponding Kalman Filter. For the synthesis of the PMA controller $\mathbf{K}_{\mathrm{PMA}}(s)$, several fixed order system have been tested and finally a 4-th order structure demonstrated to be sufficient to obtain the required level of performance without no remarkable performance improvement for higher order. A random start option has been used with the MATLAB routine *systune* to get an optimal first guess.

The optimal design of the two-stages active micro-vibration control can be also visualized in the frequency domain, where the worst-case disturbance rejection can be analyzed as a function of the
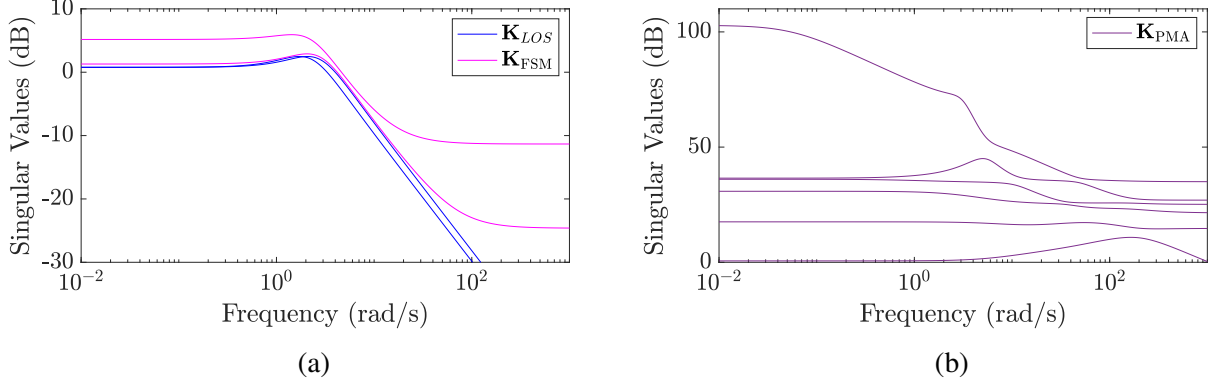
Figure 8: Fine LOS controllers: (a) Kalman filter first guess $\mathbf{K}_{LOS}$ and optimal FSM controller $\mathbf{K}_{\mathrm{FSM}}$; (b) optimal PMA controller $\mathbf{K}_{\mathrm{PMA}}$

frequency. For this purpose, Fig. 9 shows the singular values of the transfer function from all normalized input disturbance signals (both RW and SADM perturbation) to the controlled LOS. Four sets of curves are depicted in order to compare the pointing performance reached by increasing the number of adopted micro-vibrations control stages: the black lines show the transmissibility of the microvibration to the LOS in open-loop when neither passive (no isolation at payload level) nor active solutions are used; green lines depicts the same transfer functions when a passive isolator platform is introduced at the base of the payload and no active LOS control is used; magenta lines corresponds to the configuration combining the passive payload isolator together with the FSM active control stage; blue lines finally relate to the final configuration with passive isolator and double-stage LOS active control with FSM and PMAs on the isolator platform. Note that the line clouds of the same color correspond to different samples of the same uncertain closed-loop system. In the same Fig. 9 the APE and RPE specifications are illustrated as well. They all correspond to the inverse of the output filters $\mathbf{W}_{\mathrm{APE}}$, $\mathbf{W}_{\mathrm{RPE}}$ and $\mathbf{W}_{\mathrm{RPE}}^{f}$.

When a passive isolator is connected at the base of the payload, an important reduction of the propagation of the disturbance through the optical path is achieved for frequencies bigger than $\approx 500\,\mathrm{rad/s}$ (green line). As already seen in Fig. 4, this strategy allows for a reduction of micro-vibration propagation at very high frequency while introducing some extra modes at lower frequencies due to the isolator stiffness. Only an active control strategy can then reduce the impact of these modes. The use of an FSM drastically improves the pointing performance by dropping the APE below $10\,\mathrm{arcsec}$ and the RPE below $100\,\mathrm{marcsec}$ for frequencies above $100\,\mathrm{rad/s}$. A further improvement of the RPE is achieved with the use of a set of PMAs connected to the payload isolator (blue line) with a gain of almost $8\,\mathrm{dB}$ along all frequencies and guarantees a LOS error below $40\,\mathrm{marcsec}$ for frequencies above $200\,\mathrm{rad/s}$.

It is to be stressed that all these results are robustly guaranteed for any solar array angular configuration, RW speed and modeled uncertainty on the first two SA flexible modes when both RW and SADM are kept activated during the imaging phase.

FSM Synthesis			PMA Synthesis			
γ_1	γ_2	γ_3	γ_1	γ_2	γ_3	γ_4
0.7115	0.7160	0.9804	0.7115	0.7115	0.6150	0.4266

Table 2: Nominal performance of FSM and PMA control design

According to the achieved results, some lesson learned can be summed up:

- The multi-body TITOP approach allowed us to easily build an industrial benchmark by connection of some elementary blocks. From a preliminary design point of view, this assembling strategy is convenient to analyze the transmissibility of vibrations at any point of a complex system and possibly propose a different system layout by easily displacing/adding/removing the constitutive sub-structures;

- The TITOP modeling approach facilitates the choice of the set of sensors/actuators in a preliminary design phase by easily checking their efficiency at different points of the structure in the same way as described in the previous point;

- The analytical dependency of the TITOP models on their physical mechanical parameters with the LFT formalism allows the user to directly synthesize robust control laws by taking into account all the possible worst-case scenarios. This point facilitates the successive analysis of the system, that can be formally validated with analytical guarantees of system stability and performance [18] without involving time-expensive Monte Carlo campaigns;

- The proposed double-stage active micro-vibration rejection strategy allowed us to achieve very fine pointing performance. It combined a direct correction of the LOS with an FSM located in front of the sensitive instrument and a set of PMAs acting on a passive isolator, that mitigate the propagation of the microvibrations produced by the RWs and the SADM to the payload base through the most flexible elements of the spacecraft (solar panels, large mirrors of the telescope).
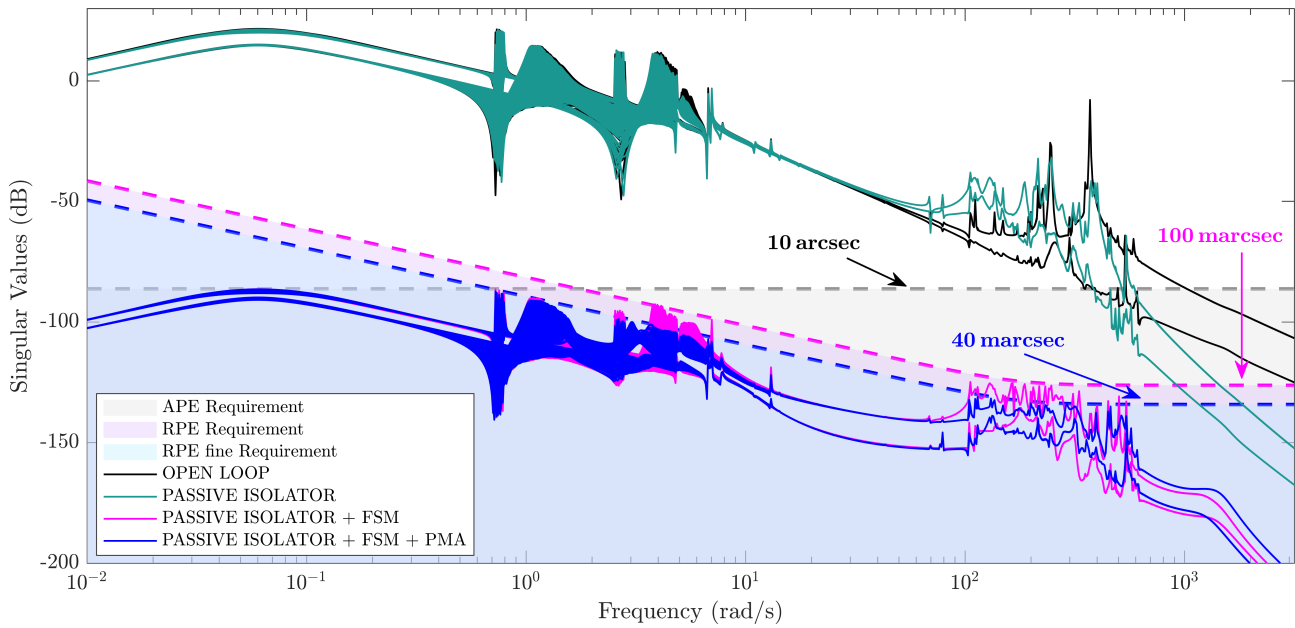
Figure 9: Singular Values of the transfer function $\begin{bmatrix} \tilde{\mathbf{w}}_{rws}^{\mathrm{T}} & \tilde{\mathbf{w}}_{sa}^{\mathrm{T}} \end{bmatrix}^{\mathrm{T}} \rightarrow \mathbf{LOS}_c$ with robust control design. Comparison of pointing performance achieved with just a payload passive isolator (green line), with a payload isolator and an FSM (magenta line) and with a payload isolator, an FSM and a set of six PMAs (blue line)

5 CONCLUSION

The Two-Input Two-Output Ports approach was used to model a complex industrial benchmark for robust line-of-sight control. Since in this framework an uncertain Linear Parametric-Varying system can be directly derived by including all possible configurations and uncertainties of the plant, two novel robust active control strategies have been proposed to mitigate the propagation of the microvibrations to the LOS error. A first one consists in synthesizing an observer of the LOS error by blending the low-frequency measurements of the LOS directly provided by a CCD camera and the accelerations measured in correspondence of the most flexible optical elements (mirrors M_1 and M_2 of a space telescope) together with the accelerations measured on a passive isolator placed at the base of the payload. An FSM then uses this information to mitigate the pointing error. In order to obtain even tighter micro-vibration attenuation, a second stage of active control was proposed as well. This strategy consists in measuring the accelerations of the payload isolator and actuating six PMAs attached to the same isolator. Thanks to this double-stage active control strategy, the propagation of the micro-vibrations induced by the RWs and SADMs is finely reduced on a very large frequency band. In particular, a reduction of the pointing error to 10 arcsec is guaranteed at low frequency (≈ 1 rad/s) with a progressive reduction of the jitter until 40 marcsec for higher frequencies where micro-vibration sources act.

This application finally allowed the authors to demonstrate the interest of the proposed modeling approach, that is able to finely capture the dynamics of a complex industrial benchmark by including all possible uncertainties in a unique LFT model. This modular framework, which permits to easily build and design a multi-body flexible structure, was in fact conceived in order to perfectly fit with the modern robust control theory. In this way the authors demonstrated how to push the control design to the limits of achievable performance, which is fundamental in the preliminary design phases of systems with very challenging pointing requirements.

REFERENCES

[1] C. Dennehy and O. S. Alvarez-Salazar, "Spacecraft Micro-Vibration: A Survey of Problems, Experiences, Potential Solutions, and Some Lessons Learned," NASA, Tech. Rep. NASA/TM-2018-220075, 2018.

[2] A. J. Bronowicki, "Vibration isolator for large space telescopes," *Journal of Spacecraft and Rockets*, vol. 43, no. 1, pp. 45–53, 2006.

[3] G. D. Racca, R. Laureijs, L. Stagnaro, J.-C. Salvignol, J. L. Alvarez, G. S. Criado, L. G. Venancio, A. Short, P. Strada, T. Bönke, C. Colombo, A. Calvi, E. Maiorano, O. Piersanti, S. Prezelus, P. Rosato, J. Pinel, H. Rozemeijer, V. Lesna, P. Musi, M. Sias, A. Anselmi, V. Cazaubiel, L. Vaillon, Y. Mellier, J. Amiaux, M. Berthé, M. Sauvage, R. Azzollini, M. Cropper, S. Pottinger, K. Jahnke, A. Ealet, T. Maciaszek, F. Pasian, A. Zacchei, R. Scaramella, J. Hoar, R. Kohley, R. Vavrek, A. Rudolph, and M. Schmidt, "The euclid mission design," *Space Telescopes and Instrumentation 2016: Optical, Infrared, and Millimeter Wave*, vol. 9904, pp. 235 – 257, 2016.

[4] L. G. Crespo, S. P. Kenny, and D. P. Giesy, "A computational framework to control verification and robustness analysis," NASA, Tech. Rep. NASA/TP-2010-216189, 2010.

[5] D. Alazard, J. A. Perez, C. Cumer, and T. Loquen, "Two-input two-output port model for mechanical systems," *AIAA Guidance, Navigation, and Control Conference*, 2015.

[6] J. Chebbi, V. Dubanchet, J. A. P. Gonzalez, and D. Alazard, "Linear dynamics of flexible multibody systems," *Multibody System Dynamics*, 2017.

[7] F. Sanfedino, D. Alazard, V. Pommier-Budinger, A. Falcoz, and F. Boquet, "Finite element based n-port model for preliminary design of multibody systems," *Journal of Sound and Vibration*, vol. 415, pp. 128–146, 2018.

[8] K. Zhou and J. C. Doyle, *Essentials of robust control*. Prentice hall Upper Saddle River, NJ, 1998.

[9] D. Alazard and F. Sanfedino, "Satellite dynamics toolbox for preliminary design phase," *43rd Annual AAS Guidance and Control Conference*, vol. 30, pp. 1461–1472, 2020.

[10] ——, "Satellite Dynamics Toolbox library (SDTlib) - User's Guide," Institut Supérieur de l'Aéronautique et de l'Espace, Tech. Rep., 2021.

[11] G. Balas, R. Chiang, A. Packard, and M. Safonov, "Robust control toolbox 3 user's guide," MATLAB, Tech. Rep., 2021.

[12] F. Sanfedino, "Experimental validation of a high accuracy pointing system," PhD Thesis, ISAE-SUPAERO, Toulouse, France, 2019.

[13] F. Sanfedino, D. Alazard, V. Preda, and D. Oddenino, "Integrated modeling of microvibrations induced by solar array drive mechanism for worst-case end-to-end analysis and robust disturbance estimation," *Mechanical Systems and Signal Processing*, vol. 163, p. 108168, 2022.

[14] F. Sanfedino, G. Thiébaud, D. Alazard, N. Guercio, and N. Deslaef, "Advances in fine line-of-sight control for large space flexible structures," *Aerospace Science and Technology*, vol. 130, p. 107961, 2022.

[15] ESA, "ESA pointing error engineering handbook," European Space Agency, Handbook ESSB-HB-E-003, 2011.

[16] P. Apkarian, P. Gahinet, and C. Buhr, "Multi-model, multi-objective tuning of fixed-structure controllers," *2014 European Control Conference (ECC)*, pp. 856–861, 2014.

[17] P. Apkarian, M. N. Dao, and D. Noll, "Parametric Robust Structured Control Design," *IEEE Transactions on Automatic Control*, vol. 60, no. 7, pp. 1857–1869, 7 2015. Available: http://ieeexplore.ieee.org/document/7027164/

[18] C. Roos, F. Lescher, J.-M. Biannic, C. Döll, and G. Ferreres, "A set of μ-analysis based tools to evaluate the robustness properties of high-dimensional uncertain systems," in *2011 IEEE International Symposium on Computer-Aided Control System Design (CACSD)*, 2011, pp. 644–649.